

UC Santa Barbara

UC Santa Barbara Previously Published Works

Title

Microstructure and dielectric properties of textured SrTiO₃ thin films

Permalink

<https://escholarship.org/uc/item/4vb7m0q0>

Journal

Journal of the American Ceramic Society, 88(4)

ISSN

0002-7820

Authors

Schmidt, S
Lu, J W
Keane, S P
et al.

Publication Date

2005-04-01

Peer reviewed

**Microstructure and dielectric properties of textured SrTiO₃
thin films**

**Steffen Schmidt, Jiwei Lu, Sean P. Keane, Lia D. Bregante, Dmitri O. Klenov
and Susanne Stemmer^{a)}**

Materials Department, University of California Santa Barbara, CA 93106-5050, USA

^{a)} Corresponding author. Electronic mail: stemmer@mrl.ucsb.edu

Abstract

We investigate the relationship between microstructure and dielectric properties of textured SrTiO₃ thin films deposited by radio-frequency magnetron sputtering on epitaxial Pt electrodes on sapphire substrates. The microstructures of Pt electrodes and SrTiO₃ films are studied by transmission electron microscopy, atomic force microscopy and x-ray diffraction. SrTiO₃ films grown on as-deposited and annealed Pt electrodes, respectively, consist of a mixture of (111) and (110) oriented grains. Temperature dependent dielectric measurements show that differences in texture and microstructure are reflected in the Curie-Weiss behavior of the SrTiO₃ films. Phenomenological models that account for the effects of thermal mismatch strain on the dielectric behavior are developed for different film textures. The models predict that at a given temperature, paraelectric (111) oriented films of SrTiO₃ on tensile substrates will have a higher Curie-Weiss temperature and a greater dielectric constant than (110) oriented films or bulk SrTiO₃. The experimental dielectric behavior is compared with the predictions from theory, and different contributions, such as interfacial layers, film stress and microstructure, to the Curie-Weiss behavior are discussed.

I. Introduction

SrTiO_3 is a prototypical soft-mode incipient ferroelectric with the perovskite structure [1, 2, 3] and is one of the best characterized complex oxides. Thin films of SrTiO_3 have long been investigated for their high dielectric constant, which is attractive for applications in integrated capacitors and for heterostructures with high- T_c superconductors [4, 5, 6, 7]. At low temperatures, SrTiO_3 shows a nonlinear, electric field tunable dielectric permittivity, which is of interest for tunable microwave devices operating at cryogenic temperatures [8, 9, 10, 11]. Large dielectric tunabilities at higher temperatures are achieved by alloying with BaTiO_3 . In contrast to pure, unstrained SrTiO_3 , $\text{Ba}_x\text{Sr}_{1-x}\text{TiO}_3$ (BST) solid solutions show a paraelectric to ferroelectric phase transformation that can be shifted to room temperature by adjusting the composition. Ferroelectric films for tunable microwave devices are used in their paraelectric phase, because of the high dielectric losses and hysteresis in the ferroelectric phase due to the motion of domains walls [11]. Heterogeneities in the Ba and Sr distribution may influence the dielectric properties of BST films [12, 13]. In contrast, SrTiO_3 thin films allow for studies of the relationships between strain, nonstoichiometry and microstructure and the dielectric properties without the influence of local variations in the composition. In addition to their practical importance, SrTiO_3 films thus represent a good model system for paraelectric, tunable dielectric thin films.

Bulk SrTiO_3 has cubic symmetry between room temperature and ~ 105 K. Below ~ 105 K it undergoes a structural (but not a ferroelectric) transition to a tetragonal phase. Above the transition temperature, the temperature (T) dependence of the dielectric susceptibility χ of bulk SrTiO_3 follows the classical Curie-Weiss-type behavior [1, 14, 15, 16, 17, 18], described by

$$\chi = \frac{\epsilon_0 C}{T - \theta} \quad (1)$$

where C is the Curie-Weiss constant, θ is the Curie-Weiss temperature and ϵ_0 the permittivity of free space.

Film nonstoichiometry, interfaces with the electrode, and film stress due to lattice and thermal mismatch with the substrate are known to strongly affect the dielectric properties and Curie-Weiss behavior of perovskite ferroelectric thin films in the paraelectric phase [13, 19, 20, 21, 22, 23, 24]. In thin films, homogeneous, biaxial film stresses are due to the thermal and lattice mismatch with the substrate. Intrinsic growth stresses can arise due to a number of factors, including point defects and grain coalescence [25, 26]. The dielectric permittivity of ferroelectric thin films often shows pronounced thickness dependence. This thickness dependence has been described with low-permittivity layers at the electrode interfaces that are connected in series with the bulk of the film [27, 28]. The origins of the thickness dependent behavior are presently not well understood, and several mechanisms have been proposed [13, 27, 29, 30, 31, 32, 33]. They include incomplete screening of the polarization by the electrodes, interfacial contamination and intrinsic deadlayer effects due to the interfacial discontinuity.

PERTSEV *et al.* and others have developed Landau-Devonshire thermodynamic models for epitaxial ferroelectric films that account for the modification of the temperature-dependent ferroelectric thin film dielectric behavior as a function of biaxial film stress [19, 34, 35]. To date, comparisons of experimental measurements with predictions from thermodynamic models have been performed for $\{001\}$ oriented, epitaxial or fiber-textured perovskite films [5, 13, 19, 36, 37, 38, 39]. For example, PERTSEV *et al.*'s model has recently been applied to explain room-temperature ferroelectricity observed in epitaxial, strained SrTiO₃ thin films [5].

Most practical capacitor structures employ metal electrodes. For example, Pt electrodes have sufficient chemical stability and a high electrical conductivity, which is required for microwave device applications [40, 41]. Perovskite films on metal electrodes are polycrystalline or textured with preferred orientations that often differ from (001) [36, 42]. The microstructure of perovskite films on metal electrodes are more complex and the relationship to the dielectric properties are less well understood than for epitaxial films. Figure 1 summarizes possible contributions of the film microstructure to the dielectric properties of polycrystalline thin films.

The goal of the present paper is to provide a better understanding of the influence of microstructure, in particular texture, film strain and grain morphology, on the dielectric properties of SrTiO₃ thin films. To realize well-defined growth surfaces for control of the SrTiO₃ film texture, Pt electrodes were grown epitaxially on sapphire substrates. Al₂O₃ is an excellent substrate for microwave devices due to its high electrical resistivity ($\sim 10^{12}$ Ω cm) and the availability of large, low cost wafers. SrTiO₃ films with different textures and grain sizes are obtained by changing the morphology of the underlying Pt electrodes.

This paper is organized as follows: after a description of the experimental methods, we briefly discuss the experimentally observed orientation relationships of epitaxial Pt electrodes on (0001) sapphire. Next, the microstructure of SrTiO₃ thin films on platinized sapphire and their dielectric behavior is described. Finally, the experimentally observed dielectric behavior is compared with the predictions from thermodynamic theory, which is developed for films with different textures.

II. Experimental

100 nm thick Pt electrodes were deposited on (0001) sapphire by DC sputtering, using 25 mTorr Ar sputter gas and a sputter power of 33 W. Substrate temperatures ranged between 600 and 750 °C. To improve the radiative coupling between the heater and the transparent sapphire, the backsides of the substrates were coated with 500 nm of Ti. A post-deposition anneal of selected Pt coated sapphire substrates was performed in the same growth chamber at 800 °C for 2 hours in 25-30 mTorr Ar. SrTiO₃ films were deposited by radio-frequency (rf) magnetron sputtering from a stoichiometric SrTiO₃ target. The base pressure of the sputter chamber was less than 5×10^{-9} Torr. Sputter conditions were optimized to obtain cation stoichiometric films and low dielectric losses. The Sr/Ti cation ratios were determined by Rutherford backscattering spectrometry (RBS). The flow ratio of Ar/O₂ sputter gases was 80:20, the sputter power was 150 W and the total (Ar+O₂) gas pressure was 25 mTorr. The substrate temperature was ~ 700 °C. The film growth rate was about 0.7 nm/min. The film thicknesses in this study ranged from 33 nm to 156 nm. To allow for a direct comparison of microstructures and dielectric properties, SrTiO₃ films were deposited in the same growth run on as-deposited and annealed Pt, respectively.

X-ray diffractometry (Philips X'PERT MPD powder diffractometer) was used to analyze film and electrode textures. The film surface root mean square (RMS) roughness and grain sizes were analyzed by atomic force microscopy (AFM). Cross-section and plan-view samples for transmission electron microscopy (TEM) were prepared by conventional TEM sample preparation with 2.5 – 4 kV Ar ion-milling, as the final step (Precision Ion Polishing System, Gatan, Inc.). Selected area electron diffraction (SAD) and TEM were carried out using transmission electron microscopes operating between 120 kV and 200 kV (FEI Tecnai G2

Sphera and JEOL-2010). High-resolution TEM (HRTEM) was performed using a field-emission TEM operating at 300 kV (FEI Tecnai F30U) with a point-to-point resolution better than 0.14 nm.

Parallel plate capacitor structures for dielectric characterization were fabricated in a two-step mask process. The first mask defined the active dielectric area. SrTiO₃ films were patterned using buffered HF or diluted HF (1:1), respectively. The second mask was used to pattern 200 nm thick, electron-beam evaporated Pt top contacts by a lift-off process. After patterning of the top electrodes, a rapid thermal annealing treatment was performed at 700 °C in ultra-high purity nitrogen for 30 seconds, which significantly improved the dielectric loss behavior. The dielectric properties were measured with a 500 mV oscillating test field using an impedance analyzer (Agilent model 4294A) connected to an air coplanar probe (Cascade Microtech, Inc.). The small-signal out-of-plane dielectric constants (ϵ_r) and out-of-plane dielectric susceptibility χ_{33} were calculated from the measured capacitance C_{device} of 50 $\mu\text{m} \times 30 \mu\text{m}$ top electrodes, i.e. $\epsilon_r = C_{device} \cdot t / A \cdot \epsilon_0$ and $\epsilon_r = 1 + \chi_{33} / \epsilon_0$ where t is the SrTiO₃ film thickness determined by AFM or TEM, and A the capacitor area. Dielectric loss tangents ($\tan \delta$) were calculated from the measured device quality factor Q , i.e. $\tan \delta = Q^{-1}$.

III. Results and Discussion

(1) Pt film microstructure

Pt films grow epitaxially on (0001) sapphire. X-ray diffraction (XRD) phi-scans (Fig. 2 (a)) show six off-axis 220 reflections ($\psi = 35.3^\circ$) corresponding to a (111) orientation of Pt. The presence of six peaks in the phi scans is due to the presence of two orientation variants of Pt

that are rotated in the film plane by 180° about the Pt [111] axis. The 220 Pt reflections of each orientation variant are rotated by 30° with respect to the 01 $\bar{1}$ 2 sapphire reflections, indicating that the close-packed metal and oxygen planes are aligned with each other as described by the following orientation relationship:

$$(111)_{\text{Pt}} \parallel (0001)_{\text{Al}_2\text{O}_3} \text{ and } [01\bar{1}]_{\text{Pt}} \parallel [10\bar{1}0]_{\text{Al}_2\text{O}_3} \quad (2a)$$

$$(111)_{\text{Pt}} \parallel (0001)_{\text{Al}_2\text{O}_3} \text{ and } [11\bar{2}]_{\text{Pt}} \parallel [1\bar{2}10]_{\text{Al}_2\text{O}_3} \quad (2b)$$

Figure 3 shows schematic projections of sapphire and Pt on the basal plane and (111) plane, respectively, and the orientation relationships observed in this study. Figure 4 shows schematic cross-sectional views of the two twin-related Pt orientation variants. The two twin-related variants differ in stacking sequence along [111], i.e. ABC versus ACB (Fig. 4). The XRD rocking curve width, using the out-of-plane Pt 111 reflections, is 0.14°. Figure 5 shows a plan-view dark field ($g = 0\bar{2}2$) image of the as-deposited film that shows the two twin-related variants with grain sizes between 160 – 550 nm. The interconnected, strongly faceted microstructure has been characterized in detail by RAMANATHAN *et al.* [43]. The preferred boundary is the $\Sigma 3$ {112} symmetrical twin boundary, which is a low-energy interface in *fcc* metals, and is oriented perpendicular to the substrate surface (see also Fig. 4).

Figure 2(b) shows XRD phi-scans of Pt/sapphire samples after annealing at 800 °C. The phi-scans show three strong film peaks for both off-axis 200 ($\psi = 54.7^\circ$) and 220 reflections, indicating that the films mainly consist of a single orientation variant after annealing. Using the 01 $\bar{1}$ 2 sapphire reflections ($\psi = 57.6^\circ$) as reference, it can be seen that this orientation variant is rotated by 30° with respect to the orientation variants present in the as-deposited films, i.e. the orientation relationship is described by:

$$(111)_{\text{Pt}} \parallel (0001)_{\text{Al}_2\text{O}_3} \quad \text{and} \quad [2\bar{1}\bar{1}]_{\text{Pt}} \parallel [10\bar{1}0]_{\text{Al}_2\text{O}_3} \quad (3)$$

For this orientation variant, the close-packed oxygen and metal planes are misaligned by 30° (Fig. 3(f)). Lower intensity reflections belonging to the variants present before annealing can also be detected. The rocking curve width (Pt 111 reflection) is reduced after annealing, to ~ 0.06°. Consistent with a reduction of the out-of-plane mosaic, the RMS roughness is found to decrease after annealing, from 0.4 nm to 0.26 nm. In contrast, the off-axis reflections are broadened after annealing, indicating an increase in the in-plane mosaic, which is probably due to the residual variants.

The orientation relationship described by Eqn. (3) has previously been observed for Pt grown on (0001) sapphire by metal-organic vapor deposition (MOCVD) [44]; however most studies in the literature report epitaxial growth of Pt on sapphire with twinning about the $[111]_{\text{Pt}}$ axis and the orientation relationships described by Eqn. (2) [42, 43, 44, 45, 46, 47]. Other *fcc* metals grown on the basal plane of sapphire also show these twin-related orientation variants [48, 49]. If interatomic forces act beyond nearest neighbors, then the two-dimensional symmetry of the bulk solids, not the two-dimensional symmetry of the specific surface plane determines the selection of structural variants [50]. Both the (0001) sapphire and the (111) Pt surfaces have $3m$ symmetry and only one orientation variant should be energetically favored. The presence of twin-related orientation variants is thus still poorly understood. It has been proposed that steps on Al-terminated Al_2O_3 surfaces may be responsible [51]. However, RAMANATHAN *et al.*, who performed a careful microstructure analysis of twinned Pt films on (0001) sapphire, concluded that twin-related variants likely nucleate on the same substrate terrace [43].

Even if a single orientation variant is preferred, it is unclear why the two original variants combine to form a single-variant of a 30° rotated orientation (described Eqn. (3)), instead of

eliminating a less favored orientation variant of the as-deposited film (described by Eqns. (2)). Further investigations that are beyond of the scope of this paper are needed to identify energetically or kinetically favored orientation variants of Pt on sapphire as a function of specific annealing conditions and/or sapphire surface morphology, termination or contamination. For example, preliminary results show that annealing of as-deposited Pt films in air does not cause growth or elimination of the existing variants.

(2) *SrTiO₃ film microstructure*

Figure 6 shows bright-field plan-view TEM micrographs of SrTiO₃ thin films grown on the as-deposited and annealed Pt/Al₂O₃ substrates, respectively. On both substrates, the SrTiO₃ film microstructure in plan-view micrographs shows elongated grains as well as approximately equiaxed (in the film plane) grains. Cross-section TEM shows that the films are columnar. On the as-deposited Pt electrode (Fig. 6(a)), the diameter of the equiaxed grains is between ~ 40 – 130 nm. The lengths of the elongated grains ranges between 160 – 300 nm, with widths between 40 – 75 nm. On the annealed Pt substrates (Fig. 6(b)), the diameter of the equiaxed grains is about 35 – 100 nm. The needle-shaped grains show a bimodal distribution with smaller grain sizes that range between 200 – 340 nm in length and 70 – 90 nm in width and much larger grains that are up to 600 nm in length.

Selected area electron diffraction (SAD) of plan-view TEM samples reveals overlapping $[111]_{\text{SrTiO}_3}$ and $\langle 110 \rangle_{\text{SrTiO}_3}$ zone axis patterns (Fig. 7). Three $\langle 110 \rangle_{\text{SrTiO}_3}$ zone axis patterns are rotated in plane by 120°. The orientation relationships are described by

$$[111]_{\text{SrTiO}_3} \parallel [111]_{\text{Pt}} \text{ and } \{\bar{1}10\}_{\text{SrTiO}_3} \parallel \{\bar{1}10\}_{\text{Pt}} \quad (4)$$

$$\langle 110 \rangle_{\text{SrTiO}_3} \parallel [111]_{\text{Pt}} \text{ and } \{001\}_{\text{SrTiO}_3} \parallel \{\bar{1}10\}_{\text{Pt}} \quad (5)$$

They are schematically illustrated in Fig. 3.

SAD shows that the highly anisotropic grains seen in plan-view images of the film on the annealed Pt are mostly $\{110\}$ oriented. Additionally, weaker reflections are detected (see arrows in Fig. 7) that corresponded to a rotation of the $\{110\}$ oriented grains by $\sim 22^\circ$ away from the exact orientation relationship described by Eqn. (5). We have previously observed these orientation relationships, including $\{110\}$ grain rotations, in sputtered SrTiO_3 films on epitaxial (111) Pt [42].

The relative ratios of (111)/(110) oriented grains can be estimated by two-beam dark-field (DF) imaging, using the 101 reflections of the (111) oriented grains. Two representative DF images are shown in Fig. 8. (111) oriented grains cover $25.6 \pm 1.5\%$ of the entire area of the SrTiO_3 film grown on as-deposited Pt. For the SrTiO_3 film grown on annealed Pt, $6.5 \pm 1.9\%$ of the total area is covered by (111) oriented grains.

HRTEM images of the SrTiO_3 film grown on the as-deposited Pt show atomically abrupt grain boundaries devoid of grain boundary phases and no planar defects in the grain interiors (Fig. 9), as expected for films close to stoichiometry. Planar defects, in particular Ruddlesden-Popper type defects [52] would indicate Sr-excess [42, 53, 54], whereas amorphous grain boundary phases are typical for Ti-rich films [21, 54]. Abnormal grain growth, as is observed for the film on the annealed electrode, has been reported for both Ti and A-site excess SrTiO_3 and BaTiO_3 ceramics [55, 56]. However, it is unlikely that annealing of the underlying electrode in a vacuum chamber impacts the cation ratio of a SrTiO_3 film subsequently grown onto it. Furthermore, grain growth due to nonstoichiometry was accompanied by planar defects [42, 55, 56], which are not observed here. HRTEM does not show significant differences in grain

boundary structure or extended defect density between the films on the as-deposited and annealed electrode, respectively.

Many different textures have been reported in the literature for SrTiO₃ and BST films on platinized substrates [57, 58, 59, 60], and it is likely that the film texture is sensitive to deposition methods and conditions in addition to the substrate. Most texture studies performed in literature are not applicable to the films in this study, as they have focused on perovskites grown on Si/SiO₂/Ti/Pt substrates with Pt films that were rougher and less well-oriented than the electrodes in this study and for which diffusion of Ti through the Pt electrode [60, 61, 62, 63] may influence the texture.

While the (111) texture may be rationalized by the excellent lattice match (0.4% at room temperature) between SrTiO₃ and Pt, it has been proposed that epitaxy on (111) oriented Pt surfaces is difficult for surface energy and electrostatic reasons [60, 64]. (111) SrTiO₃ planes are polar and consist of either SrO₃⁴⁻ layers or Ti⁴⁺ layers. The (110) textured grains have a large mismatch with Pt and are also polar (consisting of either O-only planes or SrTiO planes). We have previously shown that those {110} grains that deviate by a +/- 22° in plane rotation from the orientation relationship described by Eqn. (5) form a near coincidence site lattice with Pt, albeit with a large unit cell [42]. Thus, these grains may have rotated to form a lower-energy interface configuration.

Our results show that the annealed Pt electrode, which consists mainly of a single epitaxial Pt orientation variant, promotes the growth and nucleation of {110} oriented grains, which increase in size and in relative area coverage; thus the film texture is at least in part determined by the morphology of the underlying Pt electrode. Further studies are needed to clarify whether the change in twin boundary density in the Pt electrode promotes {110} grain

growth/nucleation or whether other factors also play a role. Such factors include the reduction in surface roughness and/or the observed changes in the in- and out-of-plane mosaic of the Pt electrode. Previously investigated films that were grown under similar conditions on epitaxial, twinned Pt (with somewhat smaller domain sizes) but with a higher growth rate (by sputtering from two targets) show a much higher density of (111) grains than the films in this study and also exhibit more pronounced grain faceting [42]. The correlation between sputter rate and (111) grain density may indicate that (111) grains nucleate more easily than {110} grains. (111) oriented films are also typical for perovskite films on Pt electrodes with thin Ti surface layers [60, 63]. In summary, there is clearly a need for more experimental studies to clarify the evolution of perovskite film texture on Pt surfaces. Epitaxial Pt electrodes present opportunities for systematic growth studies.

(3) *SrTiO₃ thin film dielectric properties*

Although detailed studies of the loss behavior of these films are beyond the scope of this paper, some information on dielectric losses is needed to interpret the temperature dependent permittivity data. At low temperatures (< 200 K), device Q -factors are above 800, indicating high-quality films. Compared with single crystals, all films show an additional dielectric loss peak just below 250 K at 1 MHz (Fig. 10). This loss peak has been previously attributed to a thin film defect mode [65]. Although RBS showed that the films have a Sr/Ti ratio that is close to 1:1, the detection limit of RBS is not sufficient to detect deviations from cation stoichiometry that may cause a defect mode. Furthermore, cation site point defects (interstitials, vacancies), oxygen vacancies and impurities are also likely present, and further studies are required to identify which point defect is responsible for this loss peak. At low temperatures, losses increase

again, similar to what is observed in single crystals. In single crystals, the increase in loss around 100 K has been attributed to domain walls that appear at the cubic-to-tetragonal transformation or to defects modes that couple to the soft mode [17, 66].

Figure 11 shows the measured inverse susceptibility (ϵ_0/χ_{33}) calculated from the measured capacitance as a function of temperature for 95 nm thick SrTiO₃ films on the as-deposited and annealed Pt electrodes, respectively. In the measured temperature range, a linear Curie-Weiss type behavior is observed with no indication of a phase transformation. A slight change in slope of the inverse susceptibility vs. temperature curve is visible when the defect polarization mechanism around 250 K “freezes” out. Linear fits to the data yield negative Curie-Weiss temperatures, for reasons discussed next.

As mentioned in the Introduction, ferroelectric thin films on metal electrodes show an apparent thickness dependent capacitance that can be modeled with layers at the film/electrode interfaces that have a lower capacitance density than the bulk and are connected in series with the bulk of the film [27, 28] (Fig. 1). This thickness or interface effect causes a thickness dependent reduction of the measured Curie-Weiss temperature. It must be extracted before other contributions, such as strain or extended defects, that may affect the temperature dependent dielectric properties of the bulk of the film can be considered [13].

The measured capacitance can be modeled as having two contributions, from the bulk of the film and from the interfacial layers at the electrodes, as expressed by [27, 28]:

$$\frac{A}{C_{device}} = \frac{(t - t_i)}{\epsilon_B \epsilon_0} + \frac{2t_i}{\epsilon_i \epsilon_0} \quad (6)$$

where ϵ_B is the thickness independent dielectric constant of the bulk of the film, ϵ_i is the dielectric constant of the interfacial layer and t_i is its thickness. If the inverse capacitance density is plotted as a function of film thickness non-zero intercepts are obtained that can be used

to determine the interfacial capacitance (assuming $t \gg t_i$). Figure 12 shows inverse capacitance densities from a thickness series of films grown on as-deposited Pt electrodes. Using Eqn. (6) an average value of interfacial capacitance density is calculated at different temperatures. To ensure intrinsic behavior without contributions from defects only low temperature measurements (120 – 200 K) are used, i.e. below the loss peak seen in Fig. 10. It is interesting to note that the interfacial layer parameters are close to those obtained in ref. [28] for BST films on Pt electrodes. The inverse susceptibilities (ϵ_0/χ_{33}) after removal of the thickness dependence are shown in Fig. 11. Linear least square fits to the data below 180 K are then used to calculate the Curie-Weiss temperatures and constants for the bulk of the films (Eqn. (1)). For the film on the as-deposited Pt, θ and C are ~ 14 K and 9.42×10^4 K, respectively, and for the film on the annealed Pt electrode, θ and C are ~ 9 K and 10.7×10^4 K, respectively (Table I). Reported bulk values vary between 28 – 40 K for the Curie-Weiss temperature and 7.1×10^4 – 8.5×10^4 K for the Curie-Weiss constant [1, 14, 15, 16, 17, 18, 67, 68]. Thus, even after accounting for the thickness effect, the measured Curie-Weiss temperatures are lower than those of bulk, single crystal SrTiO₃ at temperatures above 110 K, whereas the Curie-Weiss constants are higher. In the following we discuss possible origins of the modified Curie-Weiss behavior of these films.

The use of Eqn. (6) assumes that films with different thickness have the same bulk permittivity [30]. However, films with different thickness are expected to have somewhat different microstructures, for example due to grain growth during longer deposition times needed to produce thicker films. Films with different grain sizes may have different bulk dielectric permittivities. For the SrTiO₃ films on Pt investigated in this study, AFM shows that the basic features of the film grain morphology do not change with film thickness, i.e. the films consist of a mixture of equiaxed and elongated grains. However, grain sizes are found to increase with film

thickness. For example, the average number of grains decreases from ~ 24 grains/ μm^2 for a 33 nm thick film to ~ 12 grains/ μm^2 for a 156 nm thick film on the as-deposited Pt electrode. Except for the thinnest film (33 nm), films with different thicknesses do not show significantly different loss behavior (see Fig. 10), indicating that the point defect chemistries of films with different thicknesses are similar. The lower Q values for the 33 nm film may be due to incomplete grain coalescence observed in AFM. The thickest film shows a somewhat greater loss peak at ~ 250 K (see Fig. 10). In summary, it cannot be excluded that some part of the difference between thin film and bulk Curie-Weiss temperature may be due to an incomplete removal of the thickness effect. The thickness effect does not enter the Curie-Weiss constant.

In the literature, shifts in the Curie-Weiss temperatures in thin films have been explained with a reduced polarizability due to Ti nonstoichiometry [13] and with biaxial mechanical stresses [13, 19, 20, 36]. The films investigated here do not contain excess Ti within the detection limits of our methods ($\sim 1\%$), and it is unlikely that Ti nonstoichiometry is solely responsible for the reduction in the Curie-Weiss temperature. Biaxial tensile stresses arise due to the differences in thermal expansion of the film and the substrate (assuming that the lattice mismatch is relaxed at the growth temperature) and change the stability of ferroelectric phases compared to the unstrained bulk solid. Thus, the following sections will investigate to what extent biaxial film stresses are responsible for the modified Curie-Weiss behavior in these films.

(4) *Modeling of SrTiO₃ thin film dielectric properties*

The modified Curie-Weiss behavior for the specific case of (001) oriented cubic perovskite film under biaxial stress has been treated theoretically by several authors [13, 19, 34, 35, 69], using a Landau-Ginzburg-Devonshire formalism. These thermodynamic models predict

that the Curie-Weiss temperatures are lower and the Curie-Weiss constants are larger for cubic (001) oriented SrTiO₃ films under biaxial tensile stress compared to those of bulk, unstrained SrTiO₃ [19]. However, films in this study consist of a mixture of (111) and (110) textured grains. Thus the dielectric response of these film orientations as a function of temperature must be calculated to assess whether the modified Curie-Weiss behavior is due to biaxial film stress. Recently, TAGANTSEV *et al.* have also developed the thermodynamic potential of a (111) oriented film [70]. Here we follow closely the model by PERTSEV *et al.* [19, 34] and TAGANTSEV *et al.* [70] to calculate changes in the Curie-Weiss behavior as a function of films stress for (111) and (110) oriented films.

The elastic Gibbs function G of a cubic ($m3m$ in the high-symmetry phase) ferroelectric is given in the Landau-Ginzburg-Devonshire formalism by (using Voigt notation) [70, 71]:

$$\begin{aligned}
G = & a_1(\tilde{P}_1^2 + \tilde{P}_2^2 + \tilde{P}_3^2) + a_{11}(\tilde{P}_1^4 + \tilde{P}_2^4 + \tilde{P}_3^4) + a_{12}(\tilde{P}_1^2\tilde{P}_2^2 + \tilde{P}_1^2\tilde{P}_3^2 + \tilde{P}_2^2\tilde{P}_3^2) \\
& + a_{111}(\tilde{P}_1^6 + \tilde{P}_2^6 + \tilde{P}_3^6) + a_{112}[\tilde{P}_1^4(\tilde{P}_2^2 + \tilde{P}_3^2) + \tilde{P}_3^4(\tilde{P}_1^2 + \tilde{P}_2^2) + \tilde{P}_2^4(\tilde{P}_1^2 + \tilde{P}_3^2)] \\
& + a_{123}\tilde{P}_1^2\tilde{P}_2^2\tilde{P}_3^2 - \frac{1}{2}s_{11}(\tilde{\sigma}_1^2 + \tilde{\sigma}_2^2 + \tilde{\sigma}_3^2) - s_{12}(\tilde{\sigma}_1\tilde{\sigma}_2 + \tilde{\sigma}_1\tilde{\sigma}_3 + \tilde{\sigma}_3\tilde{\sigma}_2) - \frac{1}{2}s_{44}(\tilde{\sigma}_4^2 + \tilde{\sigma}_5^2 + \tilde{\sigma}_6^2) \\
& - Q_{11}(\tilde{\sigma}_1\tilde{P}_1^2 + \tilde{\sigma}_2\tilde{P}_2^2 + \tilde{\sigma}_3\tilde{P}_3^2) - Q_{12}[\tilde{\sigma}_1(\tilde{P}_2^2 + \tilde{P}_3^2) + \tilde{\sigma}_3(\tilde{P}_1^2 + \tilde{P}_2^2) + \tilde{\sigma}_1(\tilde{P}_1^2 + \tilde{P}_3^2)] \\
& - Q_{44}(\tilde{P}_2\tilde{P}_3\tilde{\sigma}_4 + \tilde{P}_1\tilde{P}_3\tilde{\sigma}_5 + \tilde{P}_2\tilde{P}_1\tilde{\sigma}_6)
\end{aligned} \tag{7}$$

where \tilde{P}_i and $\tilde{\sigma}_i$ are the polarization and stress components specified in the crystal reference frame $(\tilde{X}_1, \tilde{X}_2, \tilde{X}_3)$ aligned with the cube axes of the material, a_i, a_{ij} , and a_{ijk} are the dielectric stiffness coefficients at constant stress, s_{ij} are the elastic compliances and Q_{ij} are the electrostrictive coupling coefficients between polarization and stress. The polarization and stress terms in Eqn. (7) may be transformed into a film reference frame (X_1, X_2, X_3) . For example $P_i = A_{ji}^T \tilde{P}_j$, where A_{ji}^T is the transpose of the frame transformation matrix defined by

$\tilde{X}_i = A_{ij}X_j$ [70]. Here, the film reference frame is a rectangular Cartesian frame with the X_3 axis perpendicular to the film/substrate interface.

For a (111) oriented film, where the X_3 axis is parallel to [111] and the X_1 axis parallel to $[1\bar{1}0]$, A_{ij} is given by [70]

$$A_{ij} = \begin{pmatrix} 1/\sqrt{2} & -1/\sqrt{2} & 0 \\ 1/\sqrt{6} & 1/\sqrt{6} & -2/\sqrt{6} \\ 1/\sqrt{3} & 1/\sqrt{3} & 1/\sqrt{3} \end{pmatrix} \quad (8)$$

For a (110) oriented film A_{ij} is given by

$$A_{ij} = \begin{pmatrix} 1 & 0 & 0 \\ 0 & 1/\sqrt{2} & -1/\sqrt{2} \\ 0 & 1/\sqrt{2} & 1/\sqrt{2} \end{pmatrix} \quad (9)$$

Following PERTSEV *et al.* the thermodynamic potential of a thin ferroelectric film on a thick substrate is given by [34]:

$$G_{eff} = G + u_1\sigma_1 + u_2\sigma_2 + u_6\sigma_6 \quad (10)$$

The mechanical boundary conditions are given by $u_1 = u_2 = u_m$, where u_m is the mismatch strain, and $\sigma_3 = \sigma_4 = \sigma_5 = 0$ and $u_6 = 0$. All of the stress components in Eqn. (10) can be eliminated by the mechanical boundary conditions and $\partial G/\partial\sigma_1 = \partial G/\partial\sigma_2 = -u_m$ and $\partial G/\partial\sigma_6 = 0$ [34]. The latter conditions follow from the minimization of G_{eff} with respect to the stress components. G_{eff} then becomes a function of only the temperature, mismatch strain and polarization. The second and higher order polarization terms can be collected, and renormalized second and higher order coefficients, a_i^* , a_{ij}^* , ... are obtained [34]. For (111) and (110) oriented films, the expressions for G_{eff} are very cumbersome. As will be shown below, to model the dielectric behavior in the paraelectric state, only a_3^* in $G_{eff} = a_1^*(P_1^2 + P_2^2) + a_3^*P_3^2 + G^{higherorder}$ will

be needed, where $G^{\text{higherorder}}$ represents the higher order terms of the polarization. For the (111) oriented film one obtains [70]

$$a_3^* = a_1 - \frac{2(2Q_{11} + 4Q_{12} - Q_{44})u_m}{4s_{11} + 8s_{12} + s_{44}} \quad (11)$$

and for the (110) oriented film one obtains

$$a_3^* = a_1 - \frac{((2Q_{11} + 4Q_{12} - Q_{44})(s_{11} - s_{12}) + Q_{12}s_{44})u_m}{2s_{11}^2 - 4s_{12}^2 + s_{11}(2s_{12} + s_{44})} \quad (12)$$

The dielectric stiffness a_1 is assumed [19] to have a temperature dependence that follows a Curie-Weiss-type law [$a_1 = (T - \theta)/2\epsilon_0 C$]. If the lattice mismatch is completely relaxed at the growth temperature, the temperature dependence of the mismatch strain u_m can be approximated as $u_m(T) = (\alpha_s - \alpha_f)(T - T_g)$ [19], where T_g is the growth temperature, and α_s and α_f are the linear thermal expansion coefficients of the substrate and the film, respectively.

The inverse small signal susceptibility is given by $\chi_{33}^{-1} = \partial G_{\text{eff}} / \partial P_3^2$ at $P_3 \rightarrow 0$ [19]. In the paraelectric phase, the in-plane polarization components (P_1 and P_2) are set to zero. The dielectric susceptibility χ_{33} should have a temperature dependence that follows a Curie-Weiss law [19]. Differentiating G_{eff} shows that the dielectric susceptibility χ_{33} of the films is given by $\chi_{33} = 1/2a_3^*$. Rearranging Eqns. (11) and (12) in the form of a Curie-Weiss law yields the modified Curie-Weiss constants and temperatures C^* and θ^* , respectively, that are listed in Table II.

To calculate the dielectric response, the following values for the materials constants are used: $\theta = 35.5$ K [1], $C = 0.80 \times 10^5$ K [1], $\bar{\alpha}_s = 7 \times 10^{-6}$ K⁻¹ [72], $\bar{\alpha}_f = 10 \times 10^{-6}$ K⁻¹ [73], $s_{11} = 3.3 \times 10^{-12}$ m²N⁻¹, $s_{12} = -0.74 \times 10^{-12}$ m²N⁻¹, $s_{44} = 8.4 \times 10^{-12}$ m²N⁻¹ [74], $Q_{11} = 0.046$ m⁴C⁻², $Q_{12} = -0.013$ m⁴C⁻², and $Q_{44} = 0.019$ m⁴C⁻² [75]. The growth temperature is 973 K. For a (111)

oriented film, a modified C^* and θ^* of 7.92×10^4 K and 45 K, respectively, are obtained. For a (110) oriented film, C^* and θ^* are 8.03×10^4 and 32 K, respectively (Table I). The reported literature values for all coefficients that enter the equations in Table II have a very large spread [5], causing uncertainty in the calculated θ^* and C^* .

The equations in Table II predict that at a given temperature, paraelectric (111) oriented films of SrTiO₃ on tensile substrates ($\alpha_s - \alpha_f < 0$) will have a greater dielectric constant than (110) oriented films or even bulk SrTiO₃ (Fig. 13). Since the electric field tunability scales with the zero-bias dielectric constant [11], (111) oriented films will also show a greater tunability. The greater the tensile stress imposed by the substrate (i.e. the smaller α_s), the larger are the dielectric constants of paraelectric (111) oriented SrTiO₃ films. The reduction in Curie-Weiss constant and temperature for the (110) oriented film reflects a suppression of the ferroelectric behavior in the out-of-plane direction. The results show that the dielectric permittivity and tunability may be optimized not only by the choice of the substrate [5, 36], but also by the film orientation.

(5) Comparison of calculated and measured dielectric properties

In the previous sections, the following possible origins for the modified Curie-Weiss behavior of thin SrTiO₃ films on sapphire were discussed: (i) incomplete removal of the thickness effect, and (ii) biaxial film stress due to the thermal mismatch with the substrate. Comparison of the experimental data with the predictions from theory are needed to evaluate to what degree other factors that may reduce the polarizability of the bulk of the film, such as point defects, growth stresses, inhomogeneous stresses or extended defects, are responsible for the modified dielectric behavior of thin films.

Thermodynamic models predict that SrTiO₃ films with a greater (110)/(111) texture ratio have smaller Curie-Weiss temperatures and larger Curie-Weiss constants. This is consistent with the lower Curie-Weiss temperature and larger Curie-Weiss constant of the film on the annealed Pt, which has a larger fraction of (110) oriented grains. For the SrTiO₃ film on the as-deposited Pt electrode, the predicted values for C^* and θ^* are 8.00×10^4 K and 35 K, respectively. For the film on the annealed Pt electrode, C^* and θ^* are predicted to be 8.02×10^4 K and 33 K (Table I). Given the uncertainty in the estimates of the area fractions of the differently oriented grains, the measured difference in Curie-Weiss temperature (5 K) is very close to the calculated difference (2 K). The *differences* in the Curie-Weiss temperatures measured for the two films can therefore be attributed mostly to film stress, which couples differently with their different texture. It appears that for high-quality films, the *difference* in grain size and morphology between the two films, i.e. somewhat larger grain sizes in the film on the annealed Pt, has only a small (if any) influence on the Curie-Weiss temperature.

In contrast, the *absolute*, experimental values for the Curie-Weiss temperatures for both films are lower than the predicted ones. This may be in part due to the errors in the extraction of the thickness effect, as discussed in section III.(3), and due to uncertainties in the materials coefficients used in the model in section III.(4). For typical film thicknesses of interest for integrated capacitors, the thickness effect represents by far the largest contribution to experimentally observed shifts in the Curie-Weiss temperature relative to the bulk material. In contrast, thermodynamic models predict only very moderate modifications in the Curie-Weiss behavior for films that are under moderate stress (0.3-0.4 GPa [36]) due to the thermal mismatch with the sapphire substrate. Given the magnitude of the experimentally observed shifts, other effects from the films microstructure that have not yet been accounted for in models affect the

dielectric behavior at least as much as biaxial film strain from the thermal mismatch with the substrate. Specifically, these factors may include point defects, growth stresses and space charges at grain boundaries.

The experimentally observed difference in Curie-Weiss constants ($\sim 1.3 \times 10^4$ K) is much greater than predicted from thermodynamic models that account for the effects to thermal mismatch stress (~ 200 K). In contrast to the Curie-Weiss temperature, errors in removing the thickness effect do not enter the Curie-Weiss constant. In the literature, similarly large differences in the observed and calculated Curie-Weiss constants have been attributed to non-stoichiometry [13, 39]. Curie-Weiss constants of single-crystalline SrTiO₃ reported in the literature differ by 1.4×10^4 K [1, 14, 15, 16, 17, 18, 67, 68]. No precise microstructural origins have been identified to date that explain the differences in reported Curie-Weiss constants [76]. The large spread in bulk values, however, indicates that the Curie-Weiss constant is very sensitive to stress and defect density. Given that the composition of simultaneously deposited films should be identical, the large difference in measured Curie-Weiss constants for the two films indicate that relatively small changes in the extended defect structure strongly affect the Curie-Weiss constant, whereas models show that biaxial film strain from thermal mismatch is a relatively small contribution for the films investigated in this study.

IV. Summary and Conclusions

In summary, we have shown that SrTiO₃ films on epitaxial Pt electrodes represent a good model system to investigate the influence of strain and microstructure on the dielectric behavior of ferroelectric thin films. Small modifications in the underlying electrode structure produce quantifiable changes in the films' microstructure and dielectric properties, indicating pathways to

improved capacitor materials. Given that texture, strain, film/electrode interfaces and grain structure all modify the dielectric behavior an improved understanding of the evolution of film texture of perovskite films on platinized substrates is needed. We propose the use of epitaxial metal electrodes as templates for systematic growth studies.

A thickness effect, which causes an apparent shift in the Curie-Weiss temperature, is by far the largest contribution to the modified Curie-Weiss behavior of these films. Given its magnitude, there is clearly a need for a more unified understanding of the underlying physical origins of the thickness effect. Application of Landau-Devonshire models of the dielectric behavior to films with different textures showed that an increase in the apparent Curie-Weiss temperature is expected for (111) oriented SrTiO_3 films under biaxial tensile strain, whereas a decrease is expected for (110) oriented films. Choice of a suitable substrate and film orientation may thus be used to optimize dielectric permittivities and tunabilities. The differences in the dielectric behavior of films with different textures agree well with theoretical predictions that account for the influence of biaxial film strain due to the thermal mismatch with the substrate. Uncertainties in quantitative comparisons between experiments and theory arise from the great spread in reported materials coefficients used in the calculations, and from errors in removing the thickness effect. We estimate that, unless thermal mismatch stresses are very large, other contributions, such as growth stresses, point and extended defects, have at least as much an influence on the dielectric behavior as the thermal mismatch with the substrate. We show that defect modes are detected in films deposited by a high-energetic deposition method, even if films are of relatively high quality. An improved experimental understanding is needed of the coupling mechanisms between defects and the dielectric properties of thin films. Towards this goal, perovskite thin film deposition techniques should be developed to obtain not only

structurally perfect films but also films that have a very low concentration of point defects. The present study, consistent with findings by others [30, 65], shows that dielectric losses and permittivity must be measured over a large temperature range to obtain a correct understanding of the dielectric behavior of ferroelectric films.

Acknowledgements

S.S. would like to thank Prof. Jim Speck of UCSB and Dr. Alexander Tagantsev of EPFL for many helpful discussions. S. P. K. and L. D. B. were supported by the National Science Foundation IGERT program under Award No. DGE-9987618. Support for this research from the DOE Office of Basic Energy Sciences under grant # DE-FG03-02ER45994 is gratefully acknowledged.

References

- [1] K. A. Muller and H. Burkard, "SrTiO₃ - Intrinsic Quantum Paraelectric Below 4 K," *Phys. Rev. B* **19**[7]: 3593-3602 (1979).
- [2] R. A. Cowley, "Temperature Dependence of a Transverse Optic Mode in Strontium Titanate," *Phys. Rev. Lett.* **9**[4]: 159-161 (1962).
- [3] P. A. Fleury, J. F. Scott and J. M. Worlock, "Soft Phonon Modes and 110 Degrees K Phase Transition in SrTiO₃," *Phys. Rev. Lett.* **21**[1]: 16-19 (1968).
- [4] H. M. Christen, J. Mannhart, E. J. Williams and C. Gerber, "Dielectric Properties of Sputtered SrTiO₃ Films," *Phys. Rev. B* **49**[17]: 12095-12104 (1994).
- [5] J. H. Haeni, P. Irvin, W. Chang, R. Uecker, P. Reiche, Y. L. Li, S. Choudhury, W. Tian, M. E. Hawley, B. Craigo, A. K. Tagantsev, X. Q. Pan, S. K. Streiffer, L. Q. Chen, S. W. Kirchoefer, J. Levy and D. G. Schlom, "Room-temperature ferroelectricity in strained SrTiO₃," *Nature* **430**[7001]: 758-761 (2004).
- [6] M. Lippmaa, N. Nakagawa, M. Kawasaki, S. Ohashi, Y. Inaguma, M. Itoh and H. Koinuma, "Step-flow growth of SrTiO₃ thin films with a dielectric constant exceeding 10⁴," *Appl. Phys. Lett.* **74**[23]: 3543-3545 (1999).
- [7] H. C. Li, W. D. Si, A. D. West and X. X. Xi, "Near single crystal-level dielectric loss and nonlinearity in pulsed laser deposited SrTiO₃ thin films," *Appl. Phys. Lett.* **73**[2]: 190-192 (1998).
- [8] G. Rupprecht, R. O. Bell and B. D. Silverman, "Nonlinearity and Microwave Losses in Cubic Strontium-Titanate," *Phys. Rev.* **123**[1]: 97-98 (1961).
- [9] K. M. Johnson, "Variation of Dielectric Constant with Voltage in Ferroelectrics and Its Application to Parametric Devices," *J. Appl. Phys.* **33**[9]: 2826-2831 (1962).

- [10] K. Bethe, "Über das Mikrowellenverhalten Nichtlinearer Dielektrika," *Philips Res. Repts Suppl.*[2]: 1-145 (1970).
- [11] A. K. Tagantsev, V. O. Sherman, K. F. Astafiev, J. Venkatesh and N. Setter, "Ferroelectric materials for microwave tunable applications," *J. Electroceram.* **11**[1-2]: 5-66 (2003).
- [12] C. Hubert, J. Levy, A. C. Carter, W. Chang, S. W. Kiechoefer, J. S. Horwitz and D. B. Chrisey, "Confocal scanning optical microscopy of $\text{Ba}_x\text{Sr}_{1-x}\text{TiO}_3$ thin films," *Appl. Phys. Lett.* **71**[23]: 3353-3355 (1997).
- [13] S. K. Streiffner, C. Basceri, C. B. Parker, S. E. Lash and A. I. Kingon, "Ferroelectricity in thin films: The dielectric response of fiber-textured $(\text{Ba}_x\text{Sr}_{1-x})\text{Ti}_{1+y}\text{O}_{3+z}$ thin films grown by chemical vapor deposition," *J. Appl. Phys.* **86**[8]: 4565-4575 (1999).
- [14] T. Sakudo and H. Unoki, "Dielectric Properties of SrTiO_3 at Low Temperatures," *Phys. Rev. Lett.* **26**[14]: 851-853 (1971).
- [15] G. Rupprecht and R. O. Bell, "Dielectric Constant in Paraelectric Perovskites," *Physical Review A* **135**[3A]: A748-A748 (1964).
- [16] R. C. Neville, C. A. Mead and B. Hoeneisen, "Permittivity of Strontium Titanate," *J. Appl. Phys.* **43**[5]: 2124-2131 (1972).
- [17] R. Viana, P. Lunkenheimer, J. Hemberger, R. Bohmer and A. Loidl, "Dielectric-Spectroscopy in SrTiO_3 ," *Phys. Rev. B* **50**[1]: 601-604 (1994).
- [18] M. A. Saifi and L. E. Cross, "Dielectric Properties of Strontium Titanate at Low Temperature," *Phys. Rev. B* **2**[3]: 677-684 (1970).

- [19] N. A. Pertsev, A. G. Zembilgotov, S. Hoffmann, R. Waser and A. K. Tagantsev, "Ferroelectric thin films grown on tensile substrates: Renormalization of the Curie-Weiss law and apparent absence of ferroelectricity," *J. Appl. Phys.* **85**[3]: 1698-1701 (1999).
- [20] T. M. Shaw, Z. Suo, M. Huang, E. Liniger, R. B. Laibowitz and J. D. Baniecki, "The effect of stress on the dielectric properties of barium strontium titanate thin films," *Appl. Phys. Lett.* **75**[14]: 2129-2131 (1999).
- [21] S. Stemmer, S. K. Streiffer, N. D. Browning and A. I. Kingon, "Accommodation of nonstoichiometry in (100) fiber-textured $(\text{Ba}_x\text{Sr}_{1-x})\text{Ti}_{1-y}\text{O}_{3+z}$ thin films grown by chemical vapor deposition," *Appl. Phys. Lett.* **74**[17]: 2432-2434 (1999).
- [22] T. R. Taylor, P. J. Hansen, N. Pervez, B. Acikel, R. A. York and J. S. Speck, "Influence of stoichiometry on the dielectric properties of sputtered strontium titanate thin films," *J. Appl. Phys.* **94**[5]: 3390-3396 (2003).
- [23] S. Stemmer, S. K. Streiffer, N. D. Browning, C. Basceri and A. I. Kingon, "Grain boundaries in barium strontium titanate thin films: Structure, chemistry and influence on electronic properties," *Interface Sci.* **8**[2-3]: 209-221 (2000).
- [24] A. A. Sirenko, C. Bernhard, A. Golnik, A. M. Clark, J. H. Hao, W. D. Si and X. X. Xi, "Soft-mode hardening in SrTiO_3 thin films," *Nature* **404**[6776]: 373-376 (2000).
- [25] E. J. Tarsa, E. A. Hachfeld, F. T. Quinlan, J. S. Speck and M. Eddy, "Growth-related stress and surface morphology in homoepitaxial SrTiO_3 films," *Appl. Phys. Lett.* **68**[4]: 490-492 (1996).
- [26] F. Spaepen, "Interfaces and stresses in thin films," *Acta Mater.* **48**[1]: 31-42 (2000).
- [27] C. Zhou and D. M. Newns, "Intrinsic dead layer effect and the performance of ferroelectric thin film capacitor," *J. Appl. Phys.* **82**[6]: 3081-3088 (1997).

- [28] C. Basceri, S. K. Streiffer, A. I. Kingon and R. Waser, "The dielectric response as a function of temperature and film thickness of fiber-textured (Ba,Sr)TiO₃ thin films grown by chemical vapor deposition," *J. Appl. Phys.* **82**[5]: 2497-2504 (1997).
- [29] C. T. Black and J. J. Welser, "Electric-Field Penetration Into Metals: Consequences for High-Dielectric-Constant Capacitors," *IEEE Trans. Electron Dev.* **46**[4]: 776-780 (1999).
- [30] C. B. Parker, J. P. Maria and A. I. Kingon, "Temperature and thickness dependent permittivity of (Ba,Sr)TiO₃ thin films," *Appl. Phys. Lett.* **81**[2]: 340-342 (2002).
- [31] M. Dawber and J. F. Scott, "Models of electrode-dielectric interfaces in ferroelectric thin-film devices," *Jpn. J. Appl. Phys. Part 1* **41**[11B]: 6848-6851 (2002).
- [32] C. S. Hwang, "Thickness-dependent dielectric constants of (Ba,Sr)TiO₃ thin films with Pt or conducting oxide electrodes," *J. Appl. Phys.* **92**[1]: 432-437 (2002).
- [33] J. D. Baniecki, T. Shioga, K. Kurihara and N. Kamehara, "Investigation of the importance of interface and bulk limited transport mechanisms on the leakage current of high dielectric constant thin film capacitors," *J. Appl. Phys.* **94**[10]: 6741-6748 (2003).
- [34] N. A. Pertsev, A. G. Zembilgotov and A. K. Tagantsev, "Effect of mechanical boundary conditions on phase diagrams of epitaxial ferroelectric thin films," *Phys. Rev. Lett.* **80**[9]: 1988-1991 (1998).
- [35] S. B. Desu, V. P. Dudkevich, P. V. Dudkevich, I. N. Zakharchenko and G. L. Kushlyan, "Thermodynamics of Epitaxial Ferroelectric Films," *Mat. Res. Soc. Symp. Proc.* **401**: 195-201 (1996).
- [36] T. R. Taylor, P. J. Hansen, B. Acikel, N. Pervez, R. A. York, S. K. Streiffer and J. S. Speck, "Impact of thermal strain on the dielectric constant of sputtered barium strontium titanate thin films," *Appl. Phys. Lett.* **80**[11]: 1978-1980 (2002).

- [37] A. Sharma, Z. G. Ban, S. P. Alpay and J. V. Mantese, "The role of thermally-induced internal stresses on the tunability of textured barium strontium titanate films," *Appl. Phys. Lett.* **85**[6]: 985-987 (2004).
- [38] W. T. Chang, C. M. Gilmore, W. J. Kim, J. M. Pond, S. W. Kirchoefer, S. B. Qadri, D. B. Chirsey and J. S. Horwitz, "Influence of strain on microwave dielectric properties of (Ba,Sr)TiO₃ thin films," *J. Appl. Phys.* **87**[6]: 3044-3049 (2000).
- [39] K. Astafiev, V. Sherman, A. Tagantsev, N. Setter, P. Petrov, T. Kaydanova, D. Ginley, S. Hoffmann-Eifert, U. Bottger and R. Waser, "Shift of phase transition temperature in strontium titanate thin films," *Integr. Ferroelectrics* **58**: 1371-1379 (2003).
- [40] B. Acikel, T. R. Taylor, P. J. Hansen, J. S. Speck and R. A. York, "A new high performance phase shifter using Ba_xSr_{1-x}TiO₃ thin films," *IEEE Microwave & Wireless Compon. Lett.* **12**[7]: 237-239 (2002).
- [41] A. Vorobiev, P. Rundqvist, K. Khamchane and S. Gevorgian, "Silicon substrate integrated high Q-factor parallel-plate ferroelectric varactors for microwave/millimeterwave applications," *Appl. Phys. Lett.* **83**[15]: 3144-3146 (2003).
- [42] D. O. Klenov, T. R. Taylor and S. Stemmer, "SrTiO₃ films on platinized (0001) Al₂O₃: Characterization of texture and nonstoichiometry accommodation," *J. Mater. Res.* **19**[5]: 1477-1486 (2004).
- [43] S. Ramanathan, B. M. Clemens, P. C. McIntyre and U. Dahmen, "Microstructural study of epitaxial platinum and permalloy/platinum films grown on (0001) sapphire," *Philos. Mag. A* **81**[8]: 2073-2094 (2001).

- [44] R. Vargas, T. Goto, W. Zhang and T. Hirai, "Epitaxial-Growth of Iridium and Platinum Films on Sapphire by Metalorganic Chemical-Vapor-Deposition," *Appl. Phys. Lett.* **65**[9]: 1094-1096 (1994).
- [45] R. F. C. Farrow, G. R. Harp, R. F. Marks, T. A. Rabedeau, M. F. Toney, D. Weller and S. S. P. Parkin, "Epitaxial-Growth of Pt on Basal-Plane Sapphire - a Seed Film for Artificially Layered Magnetic Metal Structures," *J. Cryst. Growth* **133**[1-2]: 47-58 (1993).
- [46] H. Zhou, P. Wochner, A. Schops and T. Wagner, "Investigation of platinum films grown on sapphire (0001) by molecular beam epitaxy," *J. Cryst. Growth* **234**[2-3]: 561-568 (2002).
- [47] T. N. Blanton and L.-S. Hung, "X-ray diffraction characterization of multilayer epitaxial thin films deposited on (0001) sapphire," *The Rigaku Journal* **13**[1]: 3-7 (1996).
- [48] D. L. Medlin, K. F. McCarty, R. Q. Hwang, S. E. Guthrie and M. I. Baskes, "Orientation relationships in heteroepitaxial aluminum films on sapphire," *Thin Solid Films* **299**: 110-114 (1997).
- [49] G. Dehm, B. J. Inkson and T. Wagner, "Growth and microstructural stability of epitaxial Al films on (0001) alpha-Al₂O₃ substrates," *Acta Materialia* **50**[20]: 5021-5032 (2002).
- [50] C. P. Flynn and J. A. Eades, "Structural variants in heteroepitaxial growth," *Thin Solid Films* **389**[1-2]: 116-137 (2001).
- [51] J. Guo, H. L. M. Chang and D. J. Lam, "Substrate Surface Step Effects on Microstructure of Epitaxial Films," *Appl. Phys. Lett.* **61**[26]: 3116-3117 (1992).
- [52] S. N. Ruddlesden and P. Popper, "The Compound Sr₃Ti₂O₇ and Its Structure," *Acta Crystallographica* **11**[1]: 54-55 (1958).

- [53] R. J. D. Tilley, "An Electron Microscope Study of Perovskite-Related Oxides in Sr-Ti-O System," *J. Solid State Chem.* **21**[4]: 293-301 (1977).
- [54] T. Suzuki, Y. Nishi and M. Fujimoto, "Defect structure in homoepitaxial non-stoichiometric strontium titanate thin films," *Philos. Mag. A* **80**[3]: 621-637 (2000).
- [55] Y. K. Cho, S. J. L. Kang and D. Y. Yoon, "Dependence of grain growth and grain-boundary structure on the Ba/Ti ratio in BaTiO₃," *J. Amer. Ceram. Soc.* **87**[1]: 119-124 (2004).
- [56] S. Sturm, A. Recnik, C. Scheu and M. Ceh, "Formation of Ruddlesden-Popper faults and polytype phases in SrO-doped SrTiO₃," *J. Mater. Res.* **15**[10]: 2131-2139 (2000).
- [57] D. E. Kotecki, J. D. Baniecki, H. Shen, R. B. Laibowitz, K. L. Saenger, J. J. Lian, T. M. Shaw, S. D. Athavale, C. Cabral, P. R. Duncombe, M. Gutsche, G. Kunkel, Y. J. Park, Y. Wang and R. Wise, "(Ba,Sr)TiO₃ dielectrics for future stacked-capacitor DRAM," *IBM J. Res. Develop.* **43**[3]: 367-382 (1999).
- [58] S. M. Bilodeau, R. Carl, P. C. Van Buskirk, J. F. Roeder, C. Basceri, S. E. Lash, C. B. Parker, S. K. Streiffer and A. I. Kingon, "Dielectric properties and microstructure of thin BST films," *J. Korean Phys. Soc.* **32**: S1591-S1594 (1998).
- [59] B. A. Baumert, L. H. Chang, A. T. Matsuda, T. L. Tsai, C. J. Tracy, R. B. Gregory, P. L. Fejes, N. G. Cave, D. J. Taylor, T. Otsuki, E. Fujii, S. Hayashi and K. Suu, "Characterization of sputtered barium strontium titanate and strontium titanate thin films," *J. Appl. Phys.* **82**[5]: 2558-2566 (1997).
- [60] C. S. Hwang, M. D. Vaudin and P. K. Schenck, "Influence of the microstructure of Pt/Si substrates on textured growth of barium titanate thin films prepared by pulsed laser deposition," *J. Mater. Res.* **13**[2]: 368-375 (1998).

- [61] G. R. Fox, S. Trolrier-McKinstry, S. B. Krupanidhi and L. M. Casas, "Pt/Ti/SiO₂/Si Substrates," *J. Mater. Res.* **10**[6]: 1508-1515 (1995).
- [62] A. Ehrlich, W. Weiss, W. Hoyer and T. Gessner, "Microstructural changes of Pt/Ti bilayer during annealing in different atmospheres - An XRD study," *Thin Solid Films* **300**[1-2]: 122-130 (1997).
- [63] T. Tani, Z. Xu and D. A. Payne, "Preferred orientations for sol-gel derived PLZT thin layers," *Mat. Res. Soc. Symp. Proc.* **310**: 269-274 (1993).
- [64] P. Murali, T. Maeder, L. Sagalowicz, S. Hiboux, S. Scalese, D. Naumovic, R. G. Agostino, N. Xanthopoulos, H. J. Mathieu, L. Patthey and E. L. Bullock, "Texture control of PbTiO₃ and Pb(Zr,Ti)O₃ thin films with TiO₂ seeding," *J. Appl. Phys.* **83**[7]: 3835-3841 (1998).
- [65] C. Ang, L. E. Cross, Z. Yu, R. Guo, A. S. Bhalla and J. H. Hao, "Dielectric loss and defect mode of SrTiO₃ thin films under direct-current bias," *Appl. Phys. Lett.* **78**[18]: 2754-2756 (2001).
- [66] C. Ang, A. S. Bhalla, R. Guo and L. E. Cross, "Dielectric loss of SrTiO₃ single crystals under direct current bias," *Appl. Phys. Lett.* **76**[14]: 1929-1931 (2000).
- [67] T. Mitsui and W. B. Westphal, "Dielectric and X-Ray Studies of Ca_xBa_{1-x}TiO₃ and Ca_xSr_{1-x}TiO₃," *Phys. Rev.* **124**[5]: 1354-1359 (1961).
- [68] G. Rupprecht and R. O. Bell, "Microwave Losses in Strontium Titanate above the Phase Transition," *Phys. Rev.* **125**[6]: 1915-1920 (1962).
- [69] Z. G. Ban and S. P. Alpay, "Phase diagrams and dielectric response of epitaxial barium strontium titanate films: A theoretical analysis," *J. Appl. Phys.* **91**[11]: 9288-9296 (2002).

- [70] A. K. Tagantsev, N. A. Pertsev, P. Muralt and N. Setter, "Strain-induced diffuse dielectric anomaly and critical point in perovskite ferroelectric thin films," *Phys. Rev. B* **65**[1]: art.-no. 012104 (2002).
- [71] M. J. Haun, E. Furman, S. J. Jang, H. A. McKinstry and L. E. Cross, "Thermodynamic Theory of PbTiO_3 ," *J. Appl. Phys.* **62**[8]: 3331-3338 (1987).
- [72] R. S. Krishnan, R. Srivivasan and S. Devanarayanan (1979). *Thermal expansion of crystals*. New York, Pergamon.
- [73] D. Taylor, "Thermal-Expansion Data. 8. Complex Oxides, ABO_3 , the Perovskites," *J. Br. Ceram. Soc.* **84**[6]: 181-188 (1985).
- [74] W. Martienssen, Ed. (2002). *Ferroelectrics and Related Substances*. Landolt-Börnstein - Group III Condensed Matter. Heidelberg, Springer-Verlag.
- [75] A. K. Tagantsev, E. Courtens and L. Arzel, "Prediction of a low-temperature ferroelectric instability in antiphase domain boundaries of strontium titanate," *Phys. Rev. B* **64**[22]: art.-no. 224107 (2001).
- [76] J. F. Scott (1992). *Dielectric Properties of Insulators*. in: Encyclopedia of Applied Physics, Vol. 5. G. L. Trigg and E. H. Immergut, Eds. New York, VCH Publishers: 25-45.

Table I: Comparison of experimental and calculated values of Curie Weiss constants and temperatures for SrTiO₃ thin films on platinized sapphire.

	C^* [K]	θ^* [K]
SrTiO ₃ on as-deposited Pt after subtraction of the interfacial capacitance (experimental)	9.42×10^4	14
SrTiO ₃ on annealed Pt after subtraction of the interfacial capacitance (experimental)	10.7×10^4	9
Calculated for (111) oriented film	7.92×10^4	45
Calculated for (110) oriented film	8.03×10^4	32
Calculated for film with 26% (111) and 74% (110) oriented grains	8.00×10^4	35
Calculated for film with 7% (111) and 93% (110) oriented grains	8.02×10^4	33

Table II: Modified Curie-Weiss behavior, $\chi_{33}(T) = \epsilon_0 C^* / (T - \theta^*)$, due to biaxial mechanical film stress due to thermal mismatch with the substrate obtained from Landau-Ginzburg-Devonshire type models for epitaxial perovskite ferroelectric films with different orientations. The coefficients are defined in the text.

$$C^* = \frac{C}{1 + B \epsilon_0 C (\alpha_s - \alpha_f)} \quad \theta^* = \frac{\theta + B T_g \epsilon_0 C (\alpha_s - \alpha_f)}{1 + B \epsilon_0 C (\alpha_s - \alpha_f)}$$

where the constant B is given by

(100) oriented film^{a)}

$$B = -\frac{Q_{12}}{s_{11} + s_{12}}$$

(110) oriented film

$$B = -\frac{2((2Q_{11} + 4Q_{12} - Q_{44}) \cdot (s_{11} - s_{12}) + Q_{12} s_{44})}{2s_{11}^2 - 4s_{12}^2 + s_{11}(2s_{12} + s_{44})}$$

(111) oriented film

$$B = -\frac{4(2Q_{11} + 4Q_{12} - Q_{44})}{4s_{11} + 8s_{12} + s_{44}}$$

^{a)} see ref. [19].

FIGURE CAPTIONS

Figure 1

Schematic showing a typical microstructure of a ferroelectric thin film on a metal electrode and possible influences on the dielectric behavior.

Figure 2

(a) X-ray diffraction phi scans of the $\{222\}_{\text{Pt}}$ and $\{01\bar{1}2\}_{\text{Al}_2\text{O}_3}$ off-axis reflections recorded for the as-deposited Pt film on (0001) Al_2O_3 . The six Pt reflections are due to two different rotation variants (labeled v_1 and v_2 , respectively). (b) X-ray diffraction phi scans of the $\{222\}_{\text{Pt}}$, $\{200\}_{\text{Pt}}$ and $\{01\bar{1}2\}_{\text{Al}_2\text{O}_3}$ off-axis reflections recorded for the Pt film on (0001) Al_2O_3 after high-temperature annealing. Most of the film consists of a single orientation variant that is rotated by 30° with respect to the orientation variants in (a). Arrows indicate low-intensity reflections due to small amounts of the original variants.

Figure 3

Schematic representations of the experimentally observed orientation relationships between sapphire substrate, Pt electrodes and SrTiO_3 films with some major directions indicated. (a) Al_2O_3 structure projected on the (0001) basal plane. (b) Pt structure (fcc) projected on (111). (c) SrTiO_3 projected on (111). (d) Three different orientation variants of SrTiO_3 projected on (110). (e) Orientation relationship between Pt and sapphire for one variant in the as-deposited Pt film. (f) Main orientation relationship between Pt and sapphire after annealing (g) Orientation relationship between Pt and (111) oriented SrTiO_3 grains. (h) Orientation relationship between

Pt and (110) oriented SrTiO₃ grains. Small yellow spheres represent Al, large blue spheres O, medium green spheres Pt (differently shaded spheres represent Pt atoms at different heights along [111]), small black/grey spheres Ti and medium red spheres Sr.

Figure 4

Schematic diagrams of the Pt/sapphire interface viewed along $[10\bar{1}0]_{\text{Al}_2\text{O}_3}$, for the two different twin variants observed in the as-deposited Pt film. The translations perpendicular and parallel to the interface were chosen arbitrarily. The variant shown in (a) corresponds to an orientation relationship $[01\bar{1}]_{\text{Pt}} \parallel [10\bar{1}0]_{\text{Al}_2\text{O}_3}$ and the variant shown in (b) to $[\bar{1}1\bar{2}]_{\text{Pt}} \parallel [1\bar{2}10]_{\text{Al}_2\text{O}_3}$. Small red/yellow spheres represent Al, large blue spheres O, medium green spheres Pt.

Figure 5

Plan-view dark-field image ($\mathbf{g} = 0\bar{2}2$) of the as-deposited Pt film showing the two twin-related variants in the Pt film.

Figure 6

Plan-view bright field images of (a) the SrTiO₃ film on the as-deposited Pt electrode and (b) the SrTiO₃ film on the annealed Pt electrode.

Figure 7

Selected area electron diffraction pattern recorded from a plan-view sample of the SrTiO₃ film on the as-deposited Pt electrode. The pattern shows reflections due to (111) oriented grains (green circles) and three {110} orientation variants (connected by solid white, dashed red and

dotted blue rectangles). The relationships are $[111]_{\text{STO}} \parallel [111]_{\text{Pt}}$ and $\{\bar{1}10\}_{\text{STO}} \parallel \{\bar{1}10\}_{\text{Pt}}$ for the (111) oriented grains and $\langle 110 \rangle_{\text{STO}} \parallel [111]_{\text{Pt}}$ and $\{001\}_{\text{STO}} \parallel \{\bar{1}10\}_{\text{Pt}}$ for the $\{110\}$ oriented grains. Additional reflections belong to 22° in-plane misorientations of the $\{110\}$ grains (see arrows).

Figure 8

Plan-view dark-field images using the 101 reflections of the (111) oriented grains, which appear bright, of (a) the SrTiO₃ film on the as-deposited Pt and (b) the SrTiO₃ film on the annealed Pt.

Figure 9

Plan-view high-resolution TEM micrograph of the SrTiO₃ film on the as-deposited Pt electrode. Grain orientations are indicated in the image. Note that the film is mostly $\{110\}$ oriented. A (111) oriented grain is seen in lower left part of the image. The insets are magnified images of selected grain boundary areas that show that grain boundaries are free of amorphous phases.

Figure 10

Dielectric loss tangent ($\tan \delta$) as a function of temperature for films with different thicknesses.

Figure 11

Plots of ε_0/χ_{33} , where χ_{33} is the measured out-of-plane dielectric susceptibility, for the SrTiO₃ films on the as-deposited Pt electrode (circles) and on the annealed Pt electrode (squares). Full symbols represent as-measured data, open symbols are data after removal of the interfacial capacitance using Eqn. (6) and the thickness series shown in Fig. 12. The arrows indicate the direction of change after subtraction of the thickness effect. Solid lines through the data after

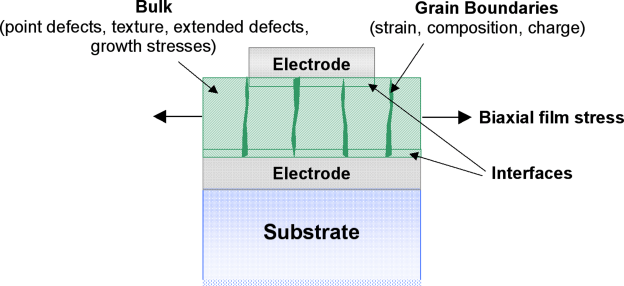
removal of the thickness effects are least-square linear fits to the data below 180 K, used to determine Curie-Weiss constant and temperature. The lines through the as-measured data are linear fits using all data points.

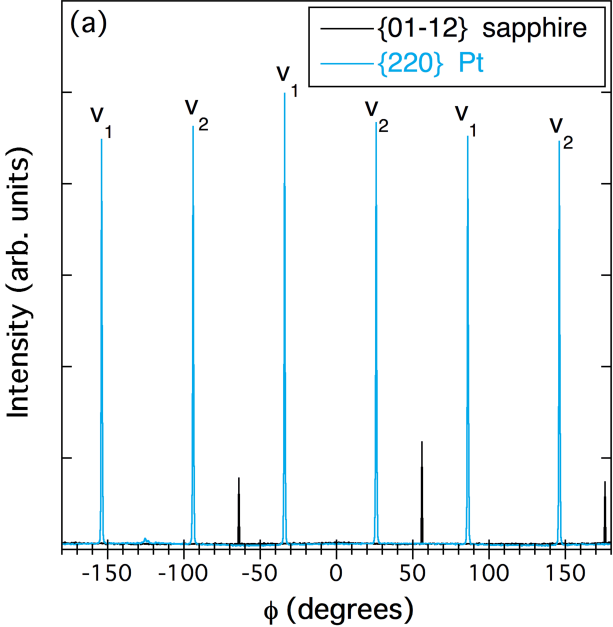
Figure 12

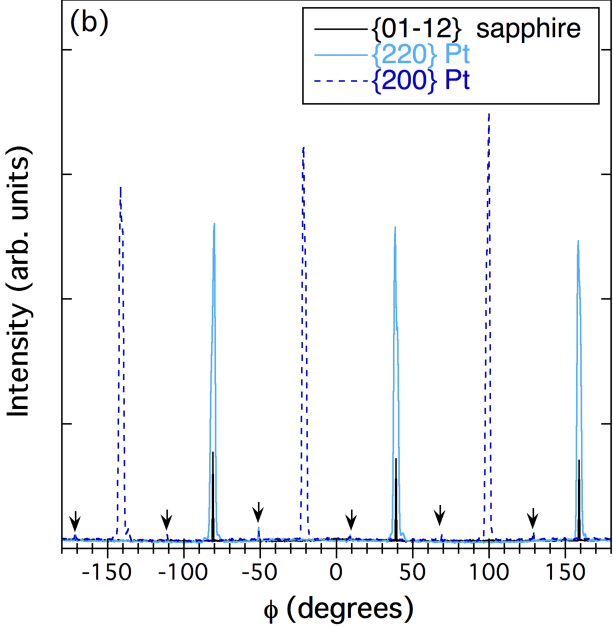
Plots the inverse capacitance density as a function of SrTiO₃ film thickness for films on the as-deposited electrodes, measured at different temperatures.

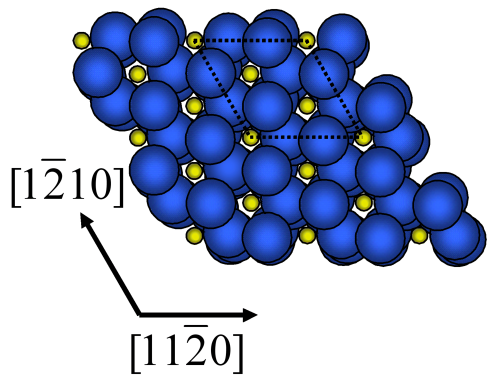
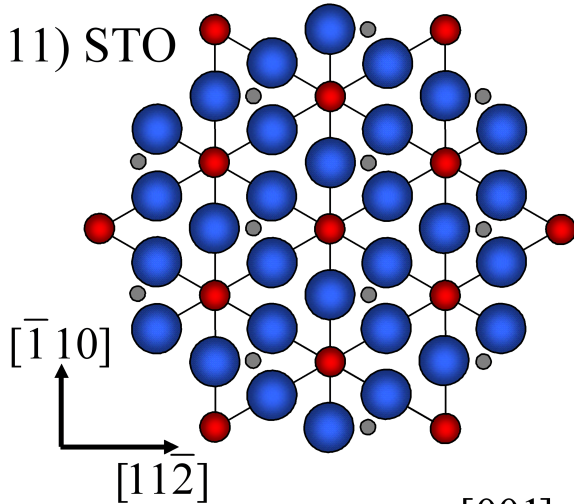
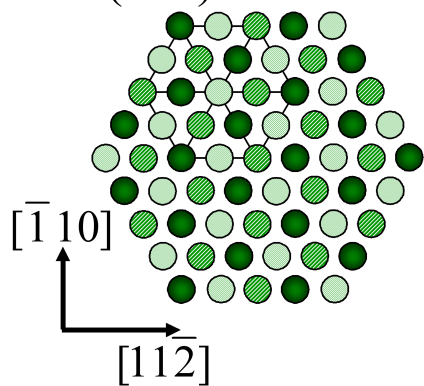
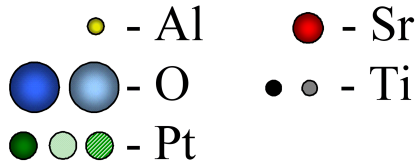
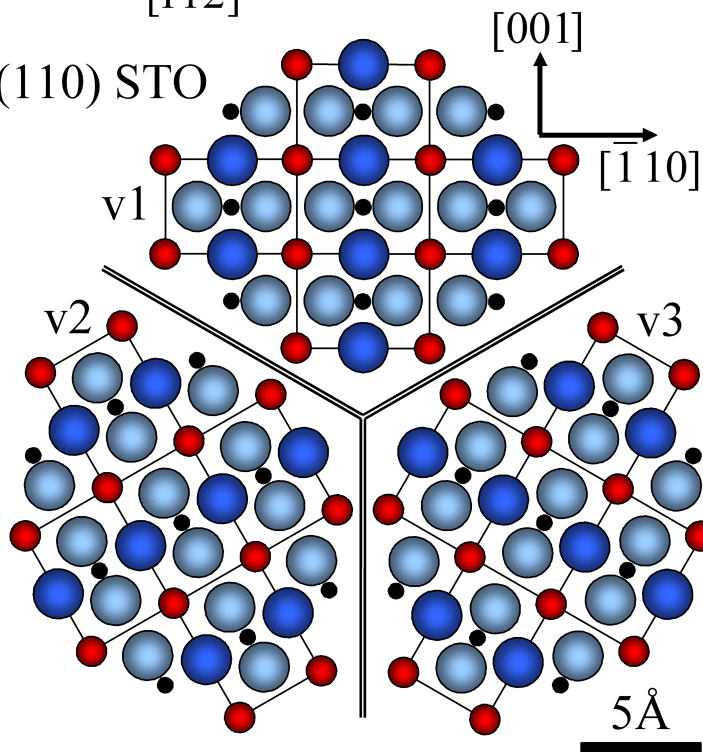
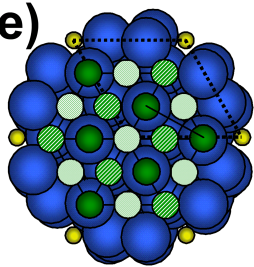
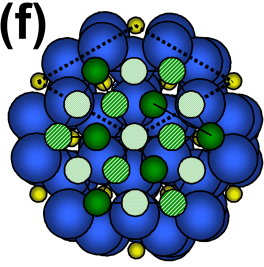
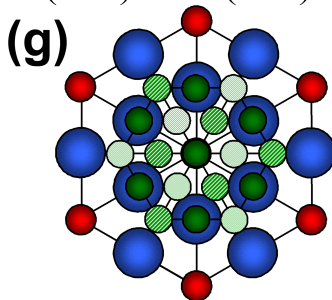
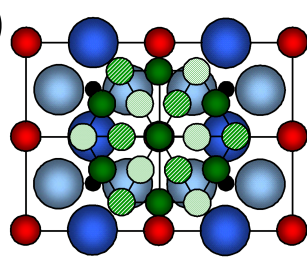
Figure 13

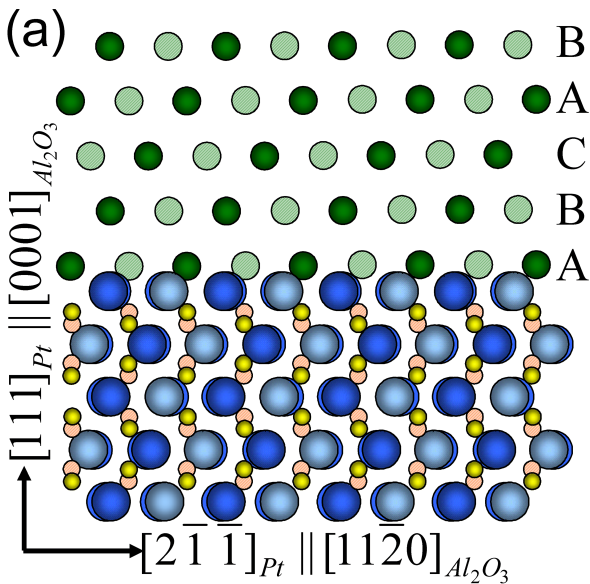
Calculated dielectric response (Curie-Weiss behavior) in the paraelectric phase of differently oriented SrTiO₃ films on Al₂O₃ substrates, respectively, calculated using the equations listed in Table II. The materials coefficients are given in the text. Depending on the phase transformation temperatures, which were not determined in this study, Curie-Weiss behavior may or may not apply in the temperature range shown.

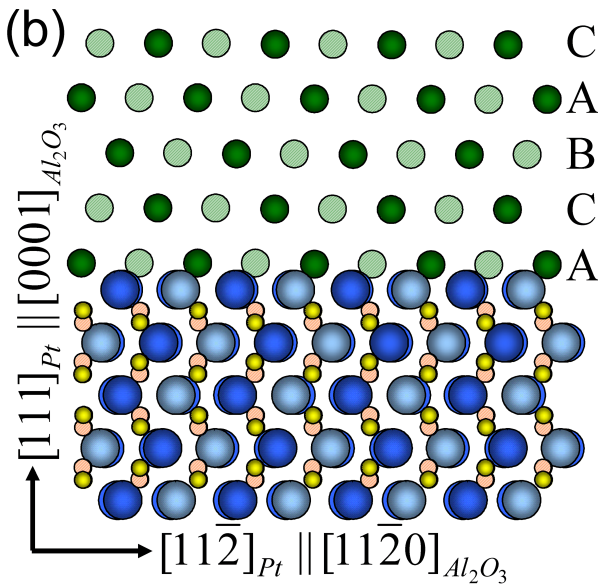


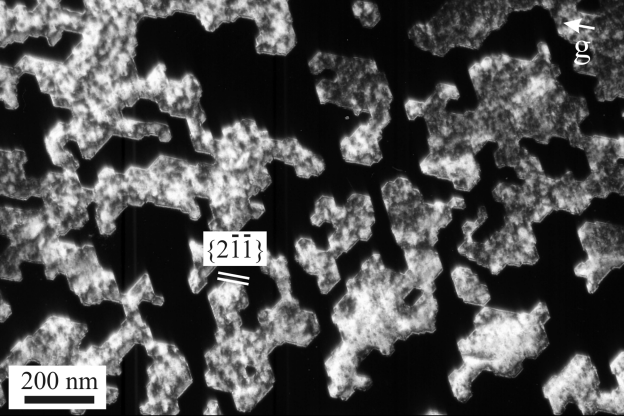




(a) (0001) Sapphire**(c)** (111) STO**(b)** (111) Platinum**(d)** (110) STO**(e)** (111)Pt/(0001)Sapphire**(f)****(g)** (111)STO/(111)Pt**(h)** (110)STO/(111)Pt**(h)**







200 nm

$\{\underline{2\bar{1}1}\}$

001 ↑

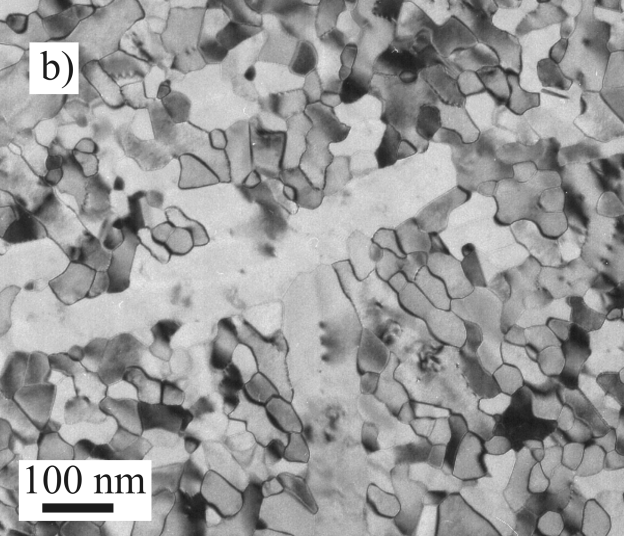
a)

100 nm

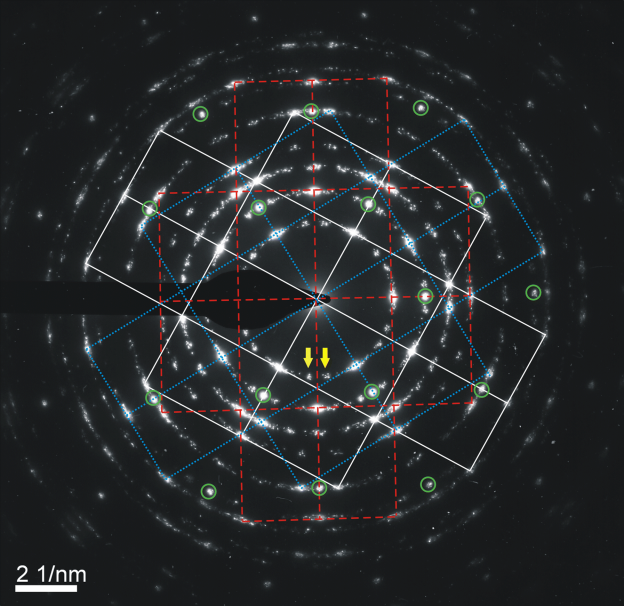


b)

100 nm



A transmission electron micrograph (TEM) showing a porous, interconnected network of dark, irregularly shaped particles. The particles are roughly spherical or polyhedral in shape and are distributed throughout a lighter, more uniform matrix. The overall structure appears to be a highly porous, interconnected network. A scale bar in the bottom left corner indicates 100 nm.



a)

200 nm



b)

200 nm



